

Variational Inference for Bayesian MIDAS Regression

Luigi Simeone*

February 2026

Abstract

We develop a Coordinate Ascent Variational Inference (CAVI) algorithm for Bayesian Mixed Data Sampling (MIDAS) regression with linear weight parameterizations. The model separates impact coefficients from weighting function parameters through a normalization constraint, creating a bilinear structure that renders generic Hamiltonian Monte Carlo samplers unreliable while preserving conditional conjugacy exploitable by CAVI. Each variational update admits a closed-form solution: Gaussian for regression coefficients and weight parameters, Inverse-Gamma for the error variance. The algorithm propagates uncertainty across blocks through second moments, distinguishing it from naive plug-in approximations. In a Monte Carlo study spanning 21 data-generating configurations with up to 50 predictors, CAVI produces posterior means nearly identical to a block Gibbs sampler benchmark while achieving speedups of $107\times$ to $1,772\times$ (Table 9). Generic automatic differentiation VI (ADVI), by contrast, produces bias 7–14 times larger while being orders of magnitude slower, confirming the value of model-specific derivations. Weight function parameters maintain excellent calibration (coverage above 92%) across all configurations. Impact coefficient credible intervals exhibit the underdispersion characteristic of mean-field approximations, with coverage declining from 89% to 55% as the number of predictors grows—a documented trade-off between speed and interval calibration that structured variational methods can address. An empirical application to realized volatility forecasting on S&P 500 daily returns confirms that CAVI and Gibbs sampling yield virtually identical point forecasts, with CAVI completing each monthly estimation in under 10 milliseconds.

Keywords: MIDAS regression, Variational inference, CAVI, Bayesian econometrics, Mixed-frequency data, Realized volatility

JEL Classification: C11, C53, C55, C63

*Independent Researcher. Contact: luigi.simeone@tech-management.net.

1 Introduction

Mixed Data Sampling (MIDAS) regression, introduced by Ghysels et al. (2006), provides a parsimonious framework for incorporating high-frequency data into low-frequency prediction equations. The approach has become standard in macroeconomic nowcasting and financial volatility forecasting, where daily or intraday observations carry information about monthly or quarterly aggregates. Bayesian treatments of MIDAS models offer natural uncertainty quantification and regularization through prior distributions—features particularly valuable when the number of high-frequency predictors is moderate to large (Mogliani and Simoni, 2021; Kohns and Potjagailo, 2025).

Posterior inference in Bayesian MIDAS models relies almost exclusively on Markov Chain Monte Carlo (MCMC) methods. The canonical framework of Chan et al. (2025) employs precision-based sampling (Chan and Jeliazkov, 2009) for time-varying parameter MIDAS with linear weight parameterizations. Pettenuzzo et al. (2016) use a four-block Gibbs sampler extending Kim-Shephard-Chib methods, while Mogliani and Simoni (2021) develop adaptive MCMC for hierarchical MIDAS with 134 predictors. These methods are asymptotically exact but computationally intensive: each posterior evaluation requires thousands of sampling iterations, and mixing efficiency degrades as the parameter space grows.

Variational inference (VI) offers a fundamentally different approach, recasting posterior approximation as an optimization problem (Blei et al., 2017). Rather than generating dependent samples from the posterior, VI seeks the closest member of a tractable distribution family by maximizing the evidence lower bound (ELBO). The resulting deterministic algorithm converges in a fraction of the time required by MCMC, producing both point estimates and approximate uncertainty quantification. When conditional conjugacy is unavailable, automatic differentiation VI (Kucukelbir et al., 2017) provides a generic black-box implementation using stochastic gradients; when the model structure permits, coordinate ascent methods yield deterministic closed-form updates. In the mixed-frequency econometrics literature, Gefang et al. (2020) demonstrated that variational Bayes methods for large mixed-frequency VARs produce accurate results while being orders of magnitude faster than MCMC. Their subsequent work (Gefang et al., 2023) extended VI to VARs with horseshoe, LASSO, and stochastic volatility specifications. Chan and Yu (2022) contributed global Gaussian variational approximations for log-volatilities in large Bayesian VARs, and Loaiza-Maya et al. (2022) developed structured variational approximations for time-varying parameter VAR models that substantially improve upon mean-field methods.

Despite this progress in mixed-frequency VARs, **variational inference has never been applied to MIDAS regression models**. This gap is methodologically significant. MIDAS regressions are structurally distinct from mixed-frequency VARs: the separation between weighting function parameters θ_j (controlling *how* high-frequency observations

are aggregated) and impact coefficients β_j (controlling *how much* each predictor matters) generates a bilinear product $\beta_j \cdot \tilde{x}_t^{(j)}(\boldsymbol{\theta}_j)$ that is absent in the VAR setting. This bilinear structure has three consequences for posterior computation that motivate the present paper.

First, generic Hamiltonian Monte Carlo (HMC) samplers—including the widely used No-U-Turn Sampler (NUTS; Hoffman and Gelman, 2014)—fail on this model. The bilinear product creates a posterior geometry analogous to Neal’s funnel (Neal, 2003): when $|\beta_j|$ is large, the posterior is tightly concentrated in $\boldsymbol{\theta}_j$; when $|\beta_j|$ is near zero, $\boldsymbol{\theta}_j$ is nearly unidentified. This curvature variation across the parameter space causes NUTS trajectories to diverge, producing biased estimates and unreliable diagnostics. Our implementation of NUTS for the MIDAS model consistently exhibited numerical divergences and non-convergent chains, confirming that off-the-shelf HMC is not a viable option.

Second, well-designed block Gibbs samplers—which condition on one parameter block at a time, collapsing the bilinear term to a linear regression—do produce valid posterior samples. However, the alternating conditional structure creates autocorrelation between successive draws that worsens with the number of predictors. In our Monte Carlo experiments, the minimum effective sample size (ESS) of the Gibbs sampler drops from 4,103 at $J = 1$ to 539 at $J = 10$ and further to 134 at $J = 25$, indicating that an increasing fraction of computational effort produces redundant samples.

Third, the very conditional structure that enables Gibbs sampling—conditional on $\boldsymbol{\theta}_j$, the model is linear in $(\alpha, \boldsymbol{\beta})$; conditional on $(\alpha, \boldsymbol{\beta})$, it is linear in each $\boldsymbol{\theta}_j$ —also enables Coordinate Ascent Variational Inference (CAVI) with closed-form updates. This is the central observation of the paper. The linear weight parameterization introduced by Chan et al. (2025)—using Almon polynomials, Fourier series, or B-splines as basis functions—maintains conditional conjugacy across all parameter blocks. We exploit this to derive a CAVI algorithm where every update step has an analytic solution: Gaussian for regression coefficients and weight parameters, Inverse-Gamma for the error variance.

Contribution. This paper makes three contributions. First, we develop the first variational inference algorithm for MIDAS regression, deriving closed-form CAVI updates that handle the bilinear structure through a mean-field factorization with variance-corrected moments. The updates propagate uncertainty across blocks via second moments—specifically, the variance of β_j enters the precision matrix of $\boldsymbol{\eta}_j$, and the variance of $\boldsymbol{\eta}_j$ enters the design matrix for $\boldsymbol{\xi}$ —producing more calibrated estimates than naive plug-in approaches. The covariance correction in the weight parameter update, arising from the joint treatment of $(\alpha, \boldsymbol{\beta})$, is a technical contribution specific to the MIDAS bilinear setting.

Second, we provide a comprehensive Monte Carlo evaluation across 21 data-generating configurations spanning $J \in \{1, 3, 5, 10, 25, 50\}$ predictors, $T \in \{50, 100, 200, 400\}$ obser-

vations, varying signal-to-noise ratios, weight profile shapes, basis function types, and frequency ratios. CAVI posterior means are nearly identical to Gibbs: bias differs by less than 0.03 across configurations, including $J = 25$ where 50 Gibbs replications confirm close agreement. Computational speedups range from $107\times$ ($J = 25$) to $1,772\times$ ($J = 1$) in the baseline tier (Table 1), reaching down to $136\times$ under stress-test conditions with $K = 65$ lags (Table 9), and grow with the number of predictors—precisely where MCMC becomes most expensive. Generic ADVI, by contrast, produces bias 7–14 times larger while being 2,000–100,000 times slower, confirming that model-specific derivations are essential. Weight function parameters ($\boldsymbol{\eta}$) maintain coverage above 92% in all configurations. Impact coefficient (β) credible intervals exhibit the underdispersion characteristic of mean-field VI, with coverage declining from 89% ($J = 1$) to 55% ($J = 50$)—a pattern we explain through the interaction between dimension-dependent cross-block correlations and the mean-field factorization.

Third, we demonstrate the method on a canonical empirical application: forecasting realized volatility of the S&P 500 using daily squared returns in a MIDAS-RV specification (Ghysels et al., 2006). Over 187 out-of-sample months, CAVI and Gibbs produce virtually identical forecasts (relative MSE difference below 0.01%), with CAVI completing each estimation in under 10 milliseconds versus 1–2.5 seconds for Gibbs.

Positioning. This paper occupies a specific niche in the literature. Relative to Chan et al. (2025), we adopt their model specification—the linear parameterization and null-space reparameterization of the normalization constraint—but replace their precision-based MCMC with variational inference. Relative to Gefang et al. (2020), we translate variational methods from mixed-frequency VARs to MIDAS regression, handling the bilinear $\beta \cdot \boldsymbol{\theta}$ structure and normalization constraint that are specific to MIDAS and absent in VARs. Relative to generic ADVI (Kucukelbir et al., 2017), our model-specific updates are both orders of magnitude faster and substantially more accurate (Section 4.5), because they exploit conditional conjugacy that stochastic gradient methods cannot leverage.

The paper proceeds as follows. Section 2 specifies the Bayesian MIDAS model. Section 3 derives the CAVI algorithm. Section 4 reports the Monte Carlo study. Section 5 presents the empirical application. Section 6 concludes.

2 Bayesian MIDAS Model

2.1 Observation equation

Consider a low-frequency dependent variable y_t , $t = 1, \dots, T$, and J high-frequency predictors. For predictor j , denote the vector of K_j high-frequency observations associated with low-frequency period t as $\mathbf{x}_t^{(j)} = (x_{t,0}^{(j)}, \dots, x_{t,K_j-1}^{(j)})^\top \in \mathbb{R}^{K_j}$. The MIDAS regression

model is

$$y_t = \alpha + \sum_{j=1}^J \beta_j \tilde{x}_t^{(j)}(\boldsymbol{\theta}_j) + \varepsilon_t, \quad \varepsilon_t \stackrel{\text{iid}}{\sim} \mathcal{N}(0, \sigma^2), \quad t = 1, \dots, T, \quad (1)$$

where α is the intercept, β_j is the impact coefficient for predictor j , and the MIDAS aggregation is

$$\tilde{x}_t^{(j)}(\boldsymbol{\theta}_j) = \sum_{k=0}^{K_j-1} w_j(k; \boldsymbol{\theta}_j) x_{t,k}^{(j)}. \quad (2)$$

The separation of β_j (how much predictor j matters) from $\boldsymbol{\theta}_j$ (how its high-frequency lags are weighted) is a defining feature of MIDAS.

2.2 Linear weight parameterization

The original MIDAS specification of Ghysels et al. (2006) employs nonlinear weighting functions—exponential Almon or beta polynomials—that create computational difficulties: the posterior conditionals of $\boldsymbol{\theta}_j$ do not belong to standard families, ruling out Gibbs sampling and requiring particle filters (Schumacher, 2014). Foroni et al. (2015) demonstrated that unrestricted lag polynomials estimated by OLS can perform comparably for small frequency ratios, motivating the shift toward linear weight specifications.

Following Chan et al. (2025), we adopt a **linear parameterization**:

$$w_j(k; \boldsymbol{\theta}_j) = \sum_{p=1}^{P_j} \theta_{j,p} \phi_p(k) = \boldsymbol{\phi}(k)^\top \boldsymbol{\theta}_j, \quad (3)$$

where $\phi_1(\cdot), \dots, \phi_{P_j}(\cdot)$ are predetermined basis functions and $\boldsymbol{\theta}_j \in \mathbb{R}^{P_j}$. Our primary specification uses **Almon polynomials**: $\phi_p(k) = k^{p-1}$. As a robustness check, we also employ cubic B-splines with uniformly spaced knots.

Using (3), the observation equation becomes

$$y_t = \alpha + \sum_{j=1}^J \beta_j \mathbf{x}_t^{(j)\top} \boldsymbol{\Phi}_j \boldsymbol{\theta}_j + \varepsilon_t, \quad (4)$$

where $\boldsymbol{\Phi}_j \in \mathbb{R}^{K_j \times P_j}$ is the basis matrix. The product $\beta_j \cdot (\mathbf{x}_t^{(j)\top} \boldsymbol{\Phi}_j \boldsymbol{\theta}_j)$ is **bilinear** in the unknown parameters β_j and $\boldsymbol{\theta}_j$ —the source of both the computational challenge and the opportunity.

Remark 1 (Negative weights). *The linear parameterization permits negative weights for certain values of $\boldsymbol{\theta}_j$, unlike nonlinear specifications. This is a trade-off: computational tractability in exchange for relaxed economic interpretability. In practice, estimated weight profiles are well-behaved, as confirmed by our Monte Carlo and empirical results.*

2.3 Normalization constraint and reparameterization

The MIDAS model in (4) suffers from a scale indeterminacy: for any $c \neq 0$, the transformation $(\beta_j, \boldsymbol{\theta}_j) \mapsto (c\beta_j, \boldsymbol{\theta}_j/c)$ leaves the likelihood invariant. The standard resolution imposes that weights sum to unity:

$$\mathbf{c}_j^\top \boldsymbol{\theta}_j = 1, \quad \text{where } \mathbf{c}_j = \boldsymbol{\Phi}_j^\top \mathbf{1}_{K_j} \in \mathbb{R}^{P_j}. \quad (5)$$

We handle this through a **null-space reparameterization** (Chan et al., 2025). Any $\boldsymbol{\theta}_j$ satisfying (5) can be decomposed as

$$\boldsymbol{\theta}_j = \boldsymbol{\theta}_j^0 + \mathbf{N}_j \boldsymbol{\eta}_j, \quad (6)$$

where $\boldsymbol{\theta}_j^0 = \mathbf{c}_j / \|\mathbf{c}_j\|^2$ is the minimum-norm particular solution, $\mathbf{N}_j \in \mathbb{R}^{P_j \times (P_j-1)}$ has orthonormal columns spanning $\ker(\mathbf{c}_j^\top)$, and $\boldsymbol{\eta}_j \in \mathbb{R}^{P_j-1}$ is the free parameter. Since $\mathbf{c}_j^\top \mathbf{N}_j = \mathbf{0}$, the constraint is automatically satisfied.

Substituting (6) into the aggregation yields

$$\tilde{x}_t^{(j)} = \underbrace{\mathbf{x}_t^{(j)\top} \boldsymbol{\Phi}_j \boldsymbol{\theta}_j^0}_{c_t^{(j)}} + \underbrace{\mathbf{x}_t^{(j)\top} \boldsymbol{\Phi}_j \mathbf{N}_j}_{\mathbf{r}_t^{(j)\top}} \boldsymbol{\eta}_j, \quad (7)$$

where $c_t^{(j)}$ is a known scalar and $\mathbf{r}_t^{(j)} \in \mathbb{R}^{P_j-1}$ is the reduced MIDAS regressor. The reparameterized model is

$$y_t = \alpha + \sum_{j=1}^J \beta_j \left[c_t^{(j)} + \mathbf{r}_t^{(j)\top} \boldsymbol{\eta}_j \right] + \varepsilon_t. \quad (8)$$

This form makes conditional linearity transparent: given $\{\boldsymbol{\eta}_j\}$, the model is linear in $\boldsymbol{\xi} = (\alpha, \beta_1, \dots, \beta_J)^\top$; given $\boldsymbol{\xi}$, it is linear in each $\boldsymbol{\eta}_j$.

2.4 Prior specification

We assign independent priors:

$$\boldsymbol{\eta}_j \sim \mathcal{N}(\mathbf{0}, \sigma_\eta^2 \mathbf{I}_{P_j-1}), \quad \sigma_\eta^2 = 1, \quad (9)$$

$$\alpha \sim \mathcal{N}(0, 100), \quad \beta_j \sim \mathcal{N}(0, 10), \quad (10)$$

$$\sigma^2 \sim \text{Inverse-Gamma}(0.01, 0.01). \quad (11)$$

The prior on $\boldsymbol{\eta}_j$ is centered at zero, corresponding to the weight profile induced by $\boldsymbol{\theta}_j^0$. The priors on α and β_j are weakly informative, and the Inverse-Gamma prior on σ^2 is the standard diffuse specification.

Remark 2 (Choice of priors). *We use identical Gaussian priors for all β_j rather than shrinkage priors. This deliberate choice isolates algorithm performance from prior specification effects. In the Monte Carlo study, null coefficients ($\beta_j = 0$) are recovered with bias below 0.005 without shrinkage. Extension to global-local shrinkage priors is straightforward.*

2.5 Posterior

The joint posterior is

$$p(\boldsymbol{\xi}, \boldsymbol{\eta}_1, \dots, \boldsymbol{\eta}_J, \sigma^2 \mid \mathbf{y}) \propto p(\mathbf{y} \mid \boldsymbol{\xi}, \boldsymbol{\eta}, \sigma^2) p(\boldsymbol{\xi}) \prod_{j=1}^J p(\boldsymbol{\eta}_j) p(\sigma^2). \quad (12)$$

Due to the bilinear terms, the marginal likelihood has no closed form. However, the **conditional posteriors** are standard: $p(\boldsymbol{\xi} \mid \boldsymbol{\eta}, \sigma^2, \mathbf{y})$ is Gaussian, each $p(\boldsymbol{\eta}_j \mid \boldsymbol{\xi}, \boldsymbol{\eta}_{-j}, \sigma^2, \mathbf{y})$ is Gaussian, and $p(\sigma^2 \mid \boldsymbol{\xi}, \boldsymbol{\eta}, \mathbf{y})$ is Inverse-Gamma.

Remark 3 (Failure of NUTS). *We attempted estimation using NUTS (Hoffman and Gelman, 2014), which operates on the joint parameter space without exploiting conditional structure. The bilinear product creates a funnel-like geometry (Neal, 2003) where posterior curvature varies by orders of magnitude. NUTS trajectories consistently produced numerical divergences, confirming that generic HMC is ill-suited to this model class.*

3 Variational Inference for MIDAS Regression

3.1 Mean-field approximation

We approximate the posterior (12) with

$$q(\boldsymbol{\xi}, \boldsymbol{\eta}_1, \dots, \boldsymbol{\eta}_J, \sigma^2) = q(\boldsymbol{\xi}) \prod_{j=1}^J q(\boldsymbol{\eta}_j) q(\sigma^2), \quad (13)$$

chosen to maximize the evidence lower bound (ELBO),

$$\mathcal{L}(q) = \mathbb{E}_q[\log p(\mathbf{y}, \boldsymbol{\xi}, \boldsymbol{\eta}, \sigma^2)] - \mathbb{E}_q[\log q(\boldsymbol{\xi}, \boldsymbol{\eta}, \sigma^2)] \leq \log p(\mathbf{y}). \quad (14)$$

The intercept and impact coefficients are kept in a **joint block $\boldsymbol{\xi}$** , preserving their posterior correlations. The weight parameters $\boldsymbol{\eta}_j$ are separated from $\boldsymbol{\xi}$ and from each other—this is the mean-field approximation that ignores cross-block correlations in exchange for tractability. Under the standard mean-field result (Blei et al., 2017), the

optimal factor q_m^* satisfies

$$\log q_m^*(\boldsymbol{\psi}_m) = \mathbb{E}_{-m}[\log p(\mathbf{y}, \boldsymbol{\psi})] + \text{const.} \quad (15)$$

3.2 Block 1: Regression coefficients

Define the effective regressor vector $\tilde{\mathbf{x}}_t = (1, \tilde{x}_t^{(1)}, \dots, \tilde{x}_t^{(J)})^\top \in \mathbb{R}^{J+1}$.

Proposition 1. *Under the mean-field factorization (13), the optimal variational distribution for the regression coefficients is $q^*(\boldsymbol{\xi}) = \mathcal{N}(\boldsymbol{\mu}_\xi, \boldsymbol{\Sigma}_\xi)$ with*

$$\boldsymbol{\Sigma}_\xi = \left(\mathbb{E}_q[\sigma^{-2}] \sum_{t=1}^T \mathbb{E}_q[\tilde{\mathbf{x}}_t \tilde{\mathbf{x}}_t^\top] + \boldsymbol{\Lambda}_\xi \right)^{-1}, \quad (16)$$

$$\boldsymbol{\mu}_\xi = \boldsymbol{\Sigma}_\xi \left(\mathbb{E}_q[\sigma^{-2}] \sum_{t=1}^T y_t \mathbb{E}_q[\tilde{\mathbf{x}}_t] \right), \quad (17)$$

where $\boldsymbol{\Lambda}_\xi = \text{diag}(\sigma_\alpha^{-2}, \sigma_\beta^{-2}, \dots, \sigma_\beta^{-2})$ is the prior precision matrix.

The required moments are $\mathbb{E}_q[\tilde{x}_t^{(j)}] = c_t^{(j)} + \mathbf{r}_t^{(j)\top} \boldsymbol{\mu}_{\eta_j}$ and

$$\mathbb{E}_q[(\tilde{x}_t^{(j)})^2] = \left(\mathbb{E}_q[\tilde{x}_t^{(j)}] \right)^2 + \mathbf{r}_t^{(j)\top} \boldsymbol{\Sigma}_{\eta_j} \mathbf{r}_t^{(j)}. \quad (18)$$

The **variance correction** term $\mathbf{r}_t^{(j)\top} \boldsymbol{\Sigma}_{\eta_j} \mathbf{r}_t^{(j)}$ propagates uncertainty about $\boldsymbol{\eta}_j$ into the update of $\boldsymbol{\xi}$, distinguishing this from a plug-in approach.

Proof. Applying the CAVI rule (15) to $\boldsymbol{\xi}$ and collecting quadratic terms from $\mathbb{E}_{-\xi}[\log p(\mathbf{y} \mid \boldsymbol{\xi}, \boldsymbol{\eta}, \sigma^2)]$ yields a Gaussian with the stated precision (16). The second-moment matrix $\mathbb{E}_q[\tilde{\mathbf{x}}_t \tilde{\mathbf{x}}_t^\top]$ arises from completing the square in $\boldsymbol{\xi}$, where the off-diagonal entries couple α and each β_j through $\mathbb{E}_q[\tilde{x}_t^{(j)}]$, and the diagonal entries involve (18). The linear term in $\boldsymbol{\xi}$ gives the mean (17). \square

3.3 Block 2: Weight parameters

For each predictor $j = 1, \dots, J$, define the partial residual

$$\bar{e}_t^{(-j)} = y_t - \mu_\alpha - \sum_{j' \neq j} \mu_{\beta_{j'}} \mathbb{E}_q[\tilde{x}_t^{(j')}] - \mu_{\beta_j} c_t^{(j)}. \quad (19)$$

Proposition 2. *Under the mean-field factorization (13), the optimal variational distri-*

bution for the weight parameters of predictor j is $q^*(\boldsymbol{\eta}_j) = \mathcal{N}(\boldsymbol{\mu}_{\eta_j}, \boldsymbol{\Sigma}_{\eta_j})$ with

$$\boldsymbol{\Sigma}_{\eta_j} = \left(\mathbb{E}_q[\sigma^{-2}] \mathbb{E}_q[\beta_j^2] \sum_{t=1}^T \mathbf{r}_t^{(j)} \mathbf{r}_t^{(j)\top} + \sigma_\eta^{-2} \mathbf{I}_{P_j-1} \right)^{-1}, \quad (20)$$

$$\boldsymbol{\mu}_{\eta_j} = \boldsymbol{\Sigma}_{\eta_j} \cdot \mathbb{E}_q[\sigma^{-2}] \left(\mu_{\beta_j} \sum_{t=1}^T \mathbf{r}_t^{(j)} \bar{e}_t^{(-j)} - \sum_{t=1}^T \mathbf{r}_t^{(j)} \mathbf{g}_t^\top \boldsymbol{\Sigma}_\xi \mathbf{e}_{j+1} \right), \quad (21)$$

where $\mathbf{g}_t = \mathbb{E}_q[\tilde{\mathbf{x}}_t]$, \mathbf{e}_{j+1} is the $(j+1)$ -th canonical basis vector, and $\mathbb{E}_q[\beta_j^2] = \mu_{\beta_j}^2 + (\boldsymbol{\Sigma}_\xi)_{j+1, j+1}$.

Three features of this update merit emphasis. *First*, the precision (20) is scaled by $\mathbb{E}_q[\beta_j^2]$, which includes the **variance** of β_j . When β_j is close to zero, the prior dominates and weights revert to the baseline—automatic regularization of irrelevant predictors.

Second, the mean (21) contains a **covariance correction** term $-\sum_t \mathbf{r}_t^{(j)} \mathbf{g}_t^\top \boldsymbol{\Sigma}_\xi \mathbf{e}_{j+1}$, arising because β_j is jointly distributed with other components of $\boldsymbol{\xi}$. Omitting this correction would ignore the benefits of the joint $(\boldsymbol{\alpha}, \boldsymbol{\beta})$ treatment.

Third, the matrix inversion in (20) has dimension $(P_j - 1) \times (P_j - 1)$, typically 2 or 3, making the per-predictor update negligible.

Proof. See Online Appendix A.1.

3.4 Block 3: Error variance

Proposition 3. *Under the mean-field factorization, the optimal variational distribution for the error variance is $q^*(\sigma^2) = \text{Inverse-Gamma}(\tilde{a}, \tilde{b})$ with*

$$\tilde{a} = a_0 + T/2, \quad \tilde{b} = b_0 + \frac{1}{2} \sum_{t=1}^T \mathbb{E}_q[e_t^2], \quad (22)$$

where $\mathbb{E}_q[e_t^2] = y_t^2 - 2y_t \mathbb{E}_q[\tilde{\mathbf{x}}_t]^\top \boldsymbol{\mu}_\xi + \text{tr}(\mathbb{E}_q[\tilde{\mathbf{x}}_t \tilde{\mathbf{x}}_t^\top] \cdot (\boldsymbol{\mu}_\xi \boldsymbol{\mu}_\xi^\top + \boldsymbol{\Sigma}_\xi))$.

Proof. Applying the CAVI rule (15) to σ^2 , the expected log-joint collects all terms involving σ^2 : the log-likelihood contributes $-\frac{T}{2} \log \sigma^2 - \frac{1}{2\sigma^2} \sum_t \mathbb{E}_q[e_t^2]$, and the Inverse-Gamma prior contributes $-(a_0 + 1) \log \sigma^2 - b_0/\sigma^2$. Combining yields the kernel of an Inverse-Gamma with the stated parameters (22). The expected squared residual $\mathbb{E}_q[e_t^2]$ expands using $\mathbb{E}_q[\boldsymbol{\xi} \boldsymbol{\xi}^\top] = \boldsymbol{\mu}_\xi \boldsymbol{\mu}_\xi^\top + \boldsymbol{\Sigma}_\xi$. \square

The moments required by other blocks are $\mathbb{E}_q[\sigma^{-2}] = \tilde{a}/\tilde{b}$ and $\mathbb{E}_q[\log \sigma^2] = \log \tilde{b} - \psi(\tilde{a})$.

3.5 The CAVI algorithm

Algorithm 1: CAVI for Bayesian MIDAS Regression

Input: Data $\{\mathbf{y}, \mathbf{x}_t^{(j)}\}$; basis matrices $\{\Phi_j\}$; hyperparameters; tolerance ε
Output: Variational parameters $\boldsymbol{\mu}_\xi, \boldsymbol{\Sigma}_\xi; \{\boldsymbol{\mu}_{\eta_j}, \boldsymbol{\Sigma}_{\eta_j}\}; \tilde{a}, \tilde{b}$; ELBO trace
Preprocessing: Compute $\boldsymbol{\theta}_j^0, \mathbf{N}_j, c_t^{(j)}, \mathbf{r}_t^{(j)}$ for all j, t ;
Initialize: $\boldsymbol{\mu}_\xi$ from OLS with uniform weights (see Appendix A.4); $\boldsymbol{\mu}_{\eta_j} = \mathbf{0}$;
 $\tilde{a} = a_0 + T/2$;
repeat
 for $j = 1, \dots, J$ **do**
 Update $q^*(\boldsymbol{\eta}_j)$ via (20)–(21);
 end
 Update $q^*(\boldsymbol{\xi})$ via (16)–(17);
 Update $q^*(\sigma^2)$ via (22);
 Compute $\mathcal{L}(q)$ via (14);
until $|\Delta\mathcal{L}|/|\mathcal{L}| < \varepsilon$;

Proposition 4 (Monotone convergence). *The ELBO sequence $\{\mathcal{L}^{(t)}\}$ generated by Algorithm 1 satisfies $\mathcal{L}^{(t+1)} \geq \mathcal{L}^{(t)}$ for all t , and converges to a fixed point.*

Proof. Each coordinate update maximizes the ELBO over the corresponding factor while holding all other factors fixed. Since the ELBO is bounded above by $\log p(\mathbf{y})$, the monotonically non-decreasing sequence converges. This is a standard property of CAVI with exponential family conditionals; see Blei et al. (2017), Section 2.4. \square

Across 10,500 CAVI fits in our Monte Carlo study, no ELBO violation was observed.

3.6 Computational complexity

The dominant cost per iteration is the $(J+1) \times (J+1)$ matrix inversion in Step 2, which is $O(J^3)$. The J inversions in Step 1 are each $(P_j - 1) \times (P_j - 1)$ —negligible for $P_j \leq 4$. Convergence requires 3–70 iterations (3 for $J = 1$, up to 70 for $J = 50$). With $T = 200$, $J = 50$, $P = 3$, a complete CAVI run takes approximately 1.4 seconds on a standard laptop.

3.7 Mean-field underdispersion

The mean-field factorization ignores $\text{Cov}(\beta_j, \boldsymbol{\eta}_j)$. This produces variational marginals more concentrated than the true posterior—underdispersion (Blei et al., 2017). The effect is **asymmetric**: the impact coefficients in $\boldsymbol{\xi}$ are correlated with all J weight vectors simultaneously, while each $\boldsymbol{\eta}_j$ is primarily correlated with its own β_j . As J grows, cumulative ignored correlations increase for $\boldsymbol{\xi}$ but remain approximately constant for each $\boldsymbol{\eta}_j$, explaining why coverage degrades for β but not for $\boldsymbol{\eta}$ (Section 4).

A partial mitigation operates through the second-moment coupling: $\mathbb{E}_q[\beta_j^2]$ in (20) propagates the uncertainty of β_j into the calibration of $\boldsymbol{\eta}_j$. No analogous mechanism compensates β_j at the individual coefficient level.

4 Monte Carlo Simulation Study

4.1 Design

We evaluate CAVI against a block Gibbs sampler across 21 DGP configurations organized in three tiers, with 500 replications each (10,500 CAVI fits; 9,500 Gibbs fits—the Gibbs sampler is omitted for $J \in \{25, 50\}$ due to prohibitive computation time). Tier 1 varies $J \in \{1, 3, 5, 10, 25, 50\}$ and $T \in \{50, 100, 200, 400\}$; Tier 2 examines weight profiles, signal-to-noise ratios, basis functions, and frequency ratios; Tier 3 contains stress tests. For configurations with $J > 1$, half the impact coefficients are zero.

4.2 Main results: scalability in J

Table 1 reports results as J increases from 1 to 50, with $T = 200$, $K = 9$, $P = 3$.

Table 1: CAVI versus Gibbs across number of predictors J . Metrics averaged over active β_j , 500 replications (50 for $J = 25$ Gibbs). Standard errors in parentheses. $T = 200$, $K = 9$, $P = 3$.

J	Method	Bias(β)	RMSE(β)	Cov95(β)	Bias(η)	Cov95(η)	Time (s)	Speedup	ESS
1	CAVI	0.029 (.007)	0.158 (.004)	0.894 (.014)	0.001 (.001)	0.929 (.011)	0.001	1,772×	—
1	Gibbs	0.032 (.007)	0.159 (.004)	0.934 (.011)	0.002 (.001)	0.936 (.011)	1.82	—	4,103
3	CAVI	0.056 (.004)	0.173 (.003)	0.836 (.017)	0.005 (.002)	0.945 (.010)	0.006	645×	—
3	Gibbs	0.078 (.004)	0.187 (.003)	0.903 (.013)	0.008 (.002)	0.957 (.009)	3.59	—	1,066
5	CAVI	0.087 (.003)	0.177 (.002)	0.594 (.022)	0.030 (.003)	0.953 (.009)	0.023	283×	—
5	Gibbs	0.103 (.003)	0.181 (.002)	0.846 (.016)	0.032 (.002)	0.974 (.007)	6.54	—	701
10	CAVI	0.079 (.003)	0.178 (.002)	0.602 (.022)	0.050 (.003)	0.963 (.010)	0.066	238×	—
10	Gibbs	0.096 (.003)	0.181 (.002)	0.850 (.016)	0.047 (.002)	0.986 (.007)	15.56	—	539
25	CAVI	0.086 (.003)	0.179 (.002)	0.581 (.022)	0.073 (.003)	0.971 (.010)	0.322	107×	—
25	Gibbs	0.159	0.186	0.828	—	—	34.44	—	134
50	CAVI	0.103 (.003)	0.196 (.003)	0.550 (.022)	0.078 (.002)	0.980 (.009)	1.383	—	—

Point estimates. Bias and RMSE are comparable between CAVI and Gibbs across all configurations where both are available. The difference in bias is at most 0.03, confirming the variational posterior mean as a reliable point estimator.

Speed. Speedup ranges from 107× ($J = 25$) to 1,772× ($J = 1$), as visualized in Figure 1. The advantage grows with dimension: at $J = 25$, CAVI completes in 0.3 seconds versus 34 seconds for Gibbs. At $J = 50$, CAVI completes in 1.4 seconds while the Gibbs sampler would require an estimated 60+ seconds (Figure 8).

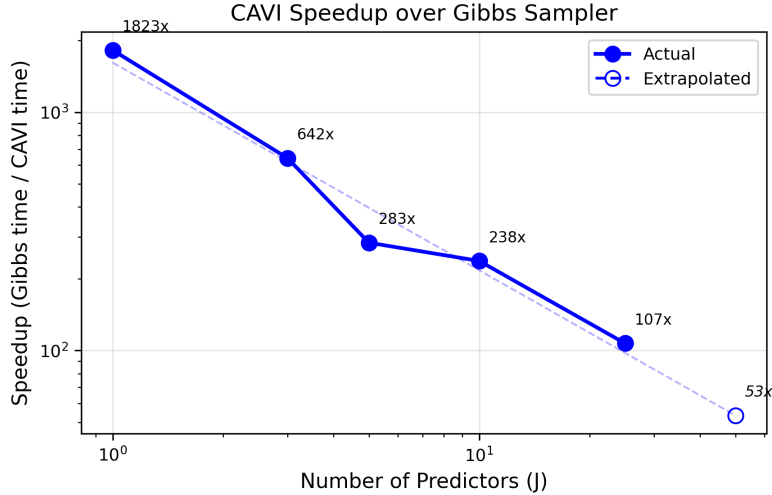


Figure 1: Computational speedup of CAVI over Gibbs sampler as a function of the number of predictors J . Solid markers: measured. Open markers: extrapolated from Gibbs scaling pattern. Even at $J = 50$, CAVI maintains a speedup of approximately $53\times$ (extrapolated).

Coverage of η . Coverage remains **above 92%** across all configurations, reaching 98% at $J = 50$. MIDAS weight profiles estimated by CAVI are well-calibrated.

Coverage of β . Coverage declines from 89.4% ($J = 1$) to 55.0% ($J = 50$), concentrated at $J \geq 5$. Two contextual observations: (i) Gibbs itself achieves only 85–93% rather than 95%, reflecting the challenging posterior geometry; (ii) the coverage gap reflects narrower intervals, not biased centers.

Gibbs ESS degradation. The minimum ESS declines from 4,103 to 539 as J grows from 1 to 10, and further to 134 at $J = 25$ (Figure 2), indicating that fewer than 5% of draws are effectively independent at $J = 25$.

4.3 Main results: sample size T

Table 2 reports results as T varies from 50 to 400, with $J = 3$.

Table 2: CAVI versus Gibbs across sample size T . 500 replications. Standard errors in parentheses. $J = 3$, $K = 9$, $P = 3$.

T	Method	Bias(β)	RMSE(β)	Cov95(β)	Bias(η)	Cov95(η)	Time (s)	Speedup	ESS
50	CAVI	0.216 (.009)	0.425 (.007)	0.584 (.022)	0.023 (.003)	0.931 (.011)	0.015	303 \times	—
50	Gibbs	0.278 (.009)	0.444 (.007)	0.807 (.018)	0.034 (.002)	0.977 (.007)	4.47	—	681
100	CAVI	0.130 (.006)	0.274 (.004)	0.729 (.020)	0.010 (.003)	0.950 (.010)	0.011	416 \times	—
100	Gibbs	0.170 (.006)	0.297 (.004)	0.860 (.016)	0.009 (.002)	0.975 (.007)	4.39	—	794
200	CAVI	0.056 (.004)	0.173 (.003)	0.836 (.017)	0.005 (.002)	0.945 (.010)	0.006	645 \times	—
200	Gibbs	0.078 (.004)	0.187 (.003)	0.903 (.013)	0.008 (.002)	0.957 (.009)	3.59	—	1,066
400	CAVI	0.028 (.003)	0.118 (.002)	0.869 (.015)	0.003 (.001)	0.932 (.011)	0.003	1,504 \times	—
400	Gibbs	0.036 (.003)	0.125 (.002)	0.929 (.012)	0.009 (.001)	0.940 (.011)	4.60	—	2,022

CAVI coverage on β increases from 58.4% ($T = 50$) to 86.9% ($T = 400$), approaching

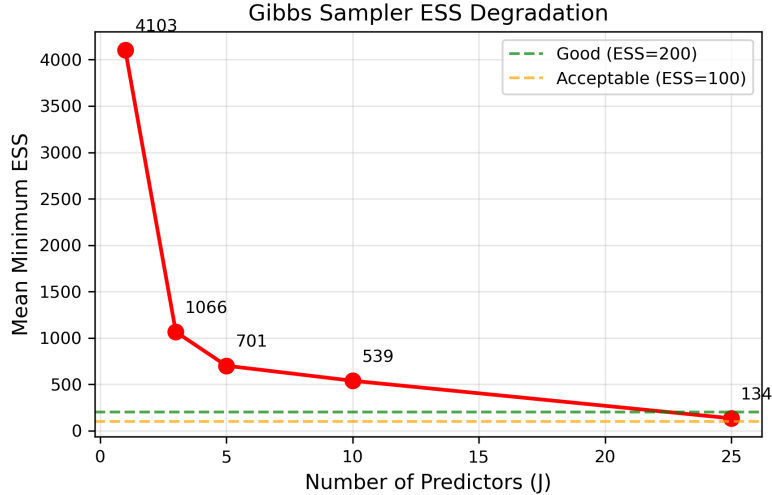


Figure 2: Gibbs sampler minimum effective sample size (ESS) as a function of J . The decline from 4,103 ($J = 1$) to 539 ($J = 10$) and further to 134 ($J = 25$, 50 replications) indicates increasing autocorrelation in the MCMC chain as bilinear coupling involves more blocks.

the Gibbs benchmark. At $T = 400$ the gap narrows to 6 percentage points. The speedup is largest when T is large: $1,504\times$ at $T = 400$, because CAVI converges in only 5 iterations while Gibbs remains at 5,000 draws. Figure 3 visualizes the coverage convergence.

4.4 Robustness and stress tests

Weight profiles (configs 2A-1 to 2A-3). Decreasing, hump-shaped, and U-shaped profiles are recovered accurately by both methods. Figure 4 illustrates the recovery for the baseline $J = 3$ configuration, confirming that CAVI and Gibbs produce nearly identical weight estimates across distinct profile shapes. Coverage on η exceeds 92% for all shapes.

Signal-to-noise ratio. High SNR ($\sigma_0^2 = 0.25$) yields 90% coverage on β for CAVI; low SNR ($\sigma_0^2 = 4$) reduces it to 75%. Gibbs coverage also declines (95% to 86%), indicating model-inherent difficulty.

Frequency ratio. At $K = 65$ (quarterly-to-daily), both CAVI and Gibbs struggle: β coverage drops to 48–50% for both, confirming a DGP/basis limitation rather than an algorithm failure.

Full robustness and stress test tables are in Online Appendix A.3.

4.5 Comparison with automatic differentiation VI

A natural question is whether generic Automatic Differentiation Variational Inference (ADVI; Kucukelbir et al., 2017) could replace our model-specific CAVI. We compare against both mean-field ADVI and full-rank ADVI implemented in PyMC 5 across $J \in \{1, 3, 5\}$ with 5 replications each (10,000 gradient steps per fit).

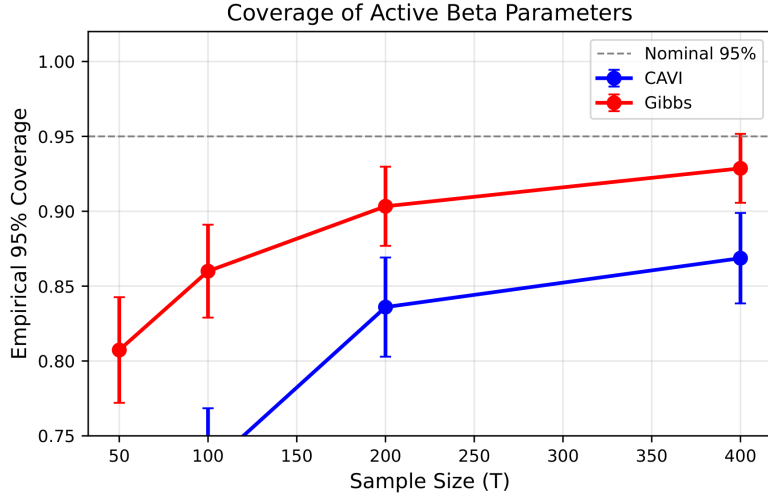


Figure 3: Empirical 95% coverage of active β_j parameters as a function of sample size T , with $J = 3$. Error bars show ± 1 standard error across replications. Both methods improve with T . The CAVI–Gibbs gap narrows from approximately 10 percentage points at $T = 100$ to 6 percentage points at $T = 400$. The $T = 50$ CAVI point (58.4%, Table 2) falls below the displayed range.

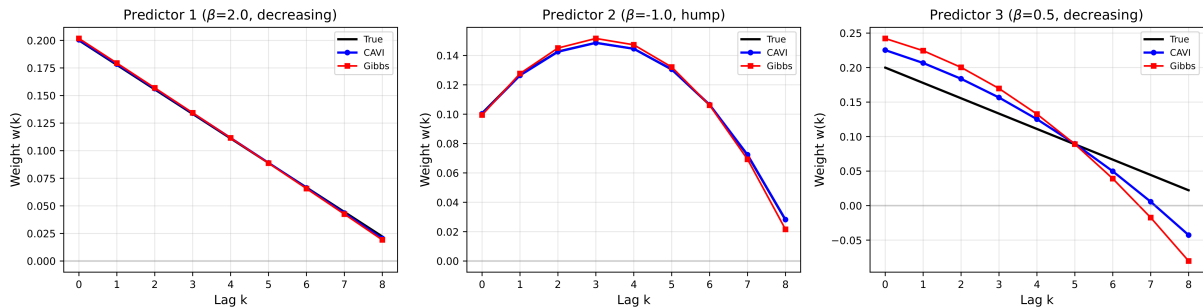


Figure 4: Weight profile recovery for a representative replication ($J = 3$, $T = 200$). Left: decreasing profile ($\beta_1 = 2.0$). Center: hump-shaped profile ($\beta_2 = -1.0$). Right: decreasing profile ($\beta_3 = 0.5$). CAVI (blue) and Gibbs (red) estimates are nearly indistinguishable from the true profile (black) for strong predictors.

Table 3: CAVI versus generic ADVI (mean-field and full-rank). 5 replications per configuration. $T = 200$, $K = 9$, $P = 3$.

J	Method	Bias(β)	RMSE(β)	Time (s)	Speedup vs ADVI-MF
1	CAVI	0.128	0.235	0.000	>100,000×
1	ADVI-MF	1.851	1.851	136.0	—
1	ADVI-FR	1.972	1.972	137.3	—
3	CAVI	0.128	0.157	0.009	24,644×
3	ADVI-MF	1.381	1.457	221.8	—
3	ADVI-FR	1.467	1.547	302.0	—
5	CAVI	0.164	0.226	0.022	1,934×
5	ADVI-MF	1.074	1.219	42.6	—
5	ADVI-FR	1.149	1.302	61.9	—

CAVI dominates ADVI on both dimensions. *Accuracy*: ADVI bias is 7–14 times larger than CAVI across all configurations, indicating that stochastic gradient optimization fails to find the correct posterior mode for the MIDAS bilinear structure. The ADVI loss function landscapes are likely plagued by the same funnel geometry that defeats NUTS. *Speed*: CAVI is 2,000–100,000 times faster. The advantage is even more dramatic than the CAVI–Gibbs comparison because ADVI requires thousands of gradient evaluations through automatic differentiation, whereas CAVI exploits closed-form conditional conjugacy.

These results confirm that the contribution of this paper is not merely computational speedup over MCMC, but the derivation of model-specific updates that exploit conditional structure unavailable to black-box methods.

4.6 Discussion

The Monte Carlo evidence supports four conclusions. First, CAVI is a reliable estimator of posterior means: bias and RMSE match Gibbs across all configurations, including $J = 25$ where the Gibbs benchmark is now available (Table 1). Second, CAVI dominates generic ADVI by a wide margin on both accuracy and speed (Table 3), confirming the value of model-specific variational derivations. Third, weight function parameters are well-calibrated (coverage $> 92\%$). Fourth, impact coefficient credible intervals exhibit mean-field underdispersion—moderate for $J \leq 3$ ($\geq 84\%$) and substantial for $J \geq 5$ ($\approx 55\text{--}60\%$).

For applications focused on point forecasting, variable selection, or weight profile estimation, CAVI offers a compelling alternative. For well-calibrated credible intervals on β in high-dimensional settings, Gibbs sampling or structured VI (Loaiza-Maya et al., 2022) should be preferred.

Practical coverage guidance. For practitioners requiring uncertainty quantification on β , we offer the following guidance based on the full Monte Carlo evidence. For $J \leq 3$ with $T \geq 200$, CAVI credible intervals achieve coverage above 83%, adequate for most applications. A simple post-hoc calibration—inflating the variational standard deviation by a multiplier κ —restores nominal coverage for $J \leq 3$: a multiplier of $\kappa = 1.2$ suffices for $J = 1$ (calibrated coverage 94.2%) and $\kappa = 1.8$ for $J = 3$ (calibrated coverage 94.9%). For $J \geq 5$, the mean-field approximation becomes inadequate for interval estimation: even a multiplier of $\kappa = 3.0$ only reaches 86% coverage at $J = 5$ and 81% at $J = 50$, because the underdispersion is non-uniform across parameters. In such settings, we recommend using the Gibbs sampler for inference on β or, when computational constraints preclude MCMC, adopting the linear response corrections of Giordano et al. (2018), which adjust variational covariances using second-order sensitivity of the ELBO. Extension to

structured variational families that capture $\text{Cov}(\beta_j, \boldsymbol{\eta}_j)$ is a natural direction for future work.

5 Empirical Application: Realized Volatility Forecasting

5.1 Setup

We apply the MIDAS-RV specification of Ghysels et al. (2006) to forecast monthly realized volatility (RV) of the S&P 500 index:

$$\log RV_t = \alpha + \beta \sum_{k=0}^{K-1} w(k; \boldsymbol{\theta}) r_{t-k}^2 + \varepsilon_t, \quad (23)$$

where $RV_t = \sum_{d=1}^{D_t} r_{t,d}^2$ is the sum of squared daily returns within month t . We use $K = 22$ daily lags and Almon polynomials with $P = 3$, and consider $J = 1$ and $J = 3$ specifications. In the $J = 3$ specification, the three predictors correspond to daily squared returns from the current month (t), the previous month ($t-1$), and two months prior ($t-2$), each aggregated with its own MIDAS weight function. Benchmarks include HAR-RV (Corsi, 2009), AR(1), AR(4), and the historical average.

Figure 5 displays the S&P 500 monthly realized volatility series from January 2000 through December 2025 (312 months, 6,537 trading days). The dashed vertical line marks the start of the out-of-sample evaluation period (187 months, expanding window from 120-month initial training sample).

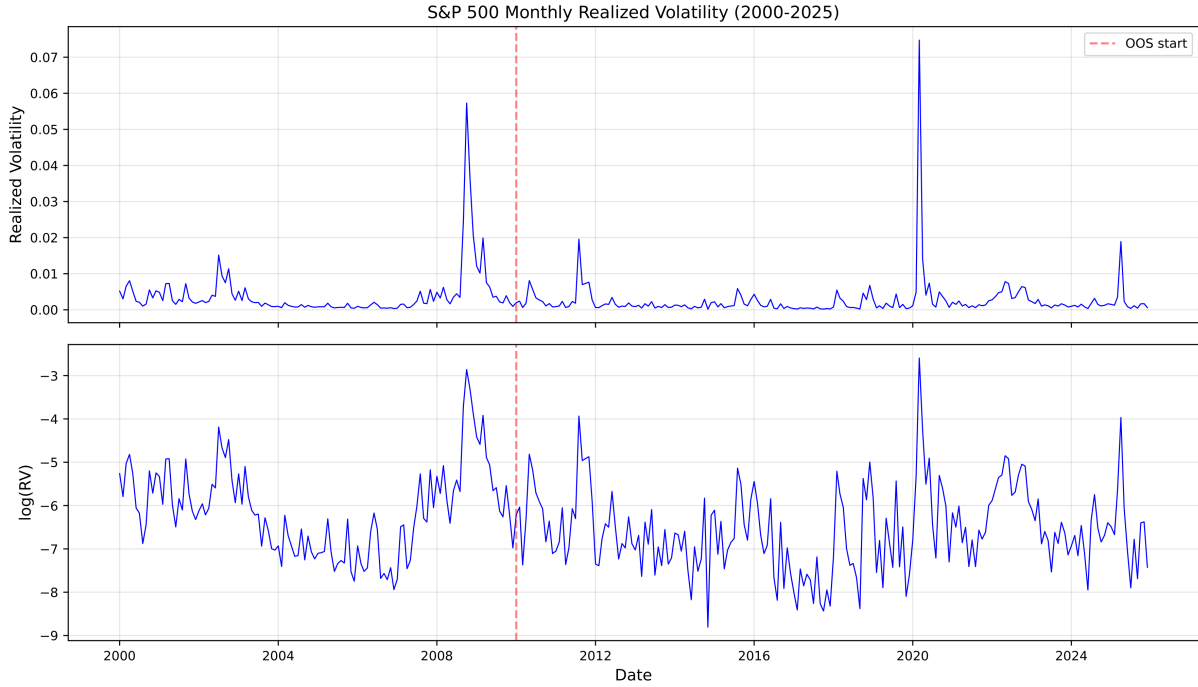


Figure 5: S&P 500 monthly realized volatility (2000–2025). Top: raw RV_t . Bottom: $\log RV_t$. Dashed line: start of out-of-sample period. Prominent spikes correspond to the 2008 financial crisis and the 2020 COVID-19 shock.

5.2 Forecast accuracy

Table 4 reports out-of-sample forecast accuracy. Diebold-Mariano tests (Diebold and Mariano, 1995) are against HAR-RV.

Table 4: Out-of-sample forecast accuracy (187 months). MSE and MAE on $\log RV_t$.

Model	MSE	MAE	Rel. MSE vs HAR	DM p -value	Time/month
MIDAS $J=1$ (CAVI)	0.720	0.651	1.058	0.226	0.001 s
MIDAS $J=1$ (Gibbs)	0.720	0.651	1.058	0.224	1.13 s
MIDAS $J=3$ (CAVI)	0.688	0.633	1.011	0.864	0.009 s
MIDAS $J=3$ (Gibbs)	0.702	0.635	1.031	0.633	2.48 s
HAR-RV	0.680	0.645	1.000	—	<0.001 s
AR(1)	0.713	0.657	1.048	0.045	<0.001 s
AR(4)	0.711	0.653	1.046	0.358	<0.001 s
Historical Avg	0.997	0.802	1.465	0.000	<0.001 s

CAVI–Gibbs agreement. The MSE difference between CAVI and Gibbs is 0.00006 for $J = 1$ (relative difference: 0.01%), confirming the Monte Carlo finding. Figure 6 shows that MIDAS $J = 1$ (CAVI) tracks the actual log-RV series closely, with performance comparable to HAR-RV.

Forecasting performance. MIDAS $J = 3$ nearly matches HAR-RV (relative MSE = 1.011; DM $p = 0.864$). Neither MIDAS specification is significantly worse than HAR at

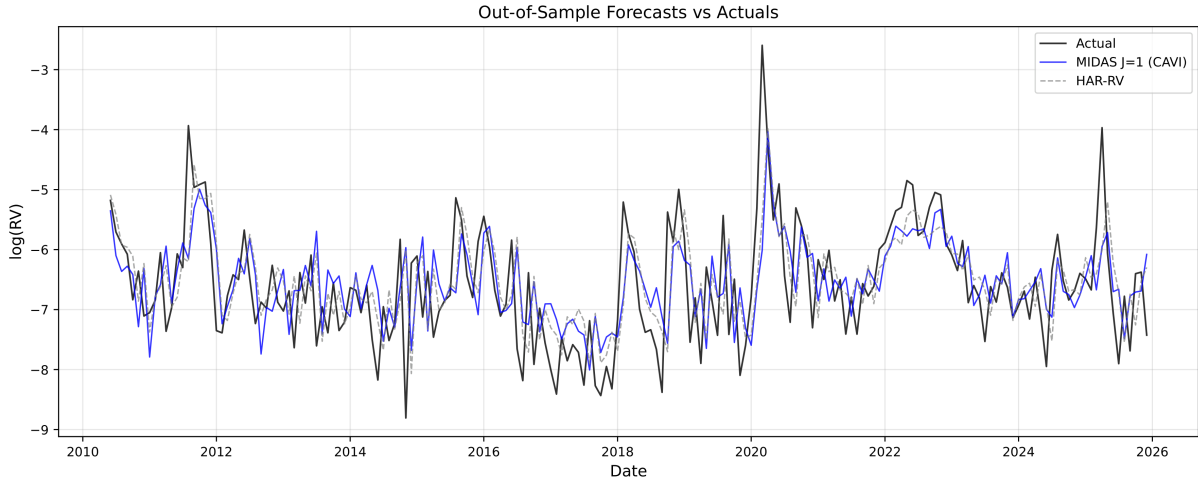


Figure 6: Out-of-sample forecasts of $\log RV_t$ (2010–2025). Black: actual. Blue: MIDAS $J = 1$ (CAVI). Gray dashed: HAR-RV. Both models track the actual series closely, with large forecast errors concentrated around the March 2020 COVID-19 volatility spike.

conventional levels, while AR(1) is significantly inferior ($p = 0.045$) and the historical average is strongly dominated ($p < 0.001$).

Computational time. CAVI completes each monthly estimation in 1 ms ($J = 1$) or 9 ms ($J = 3$), yielding speedups of $936\times$ and $264\times$ respectively. In a single-pass estimation such as this application, the absolute time difference (1–2 seconds for Gibbs) may seem inconsequential. However, the speed advantage becomes decisive in three settings that are increasingly common in applied work: (i) large-scale model comparison exercises scanning over many predictor sets, lag structures, or basis specifications; (ii) real-time nowcasting pipelines with hundreds of candidate predictors, where estimation must complete within a publication cycle; and (iii) expanding-window or rolling-window evaluations with hundreds of re-estimations, as in the present exercise (187 out-of-sample months \times multiple specifications). With $J = 10$ predictors and 500 windows, CAVI completes in approximately 33 seconds versus 2.2 hours for Gibbs.

5.3 Estimated weight profiles

Figure 7 displays the estimated MIDAS weight profile from the full-sample $J = 1$ estimation. Both CAVI and Gibbs produce a monotonically decreasing profile, assigning greatest weight to the most recent daily observations—economically sensible, as recent squared returns are more informative about current-month volatility. The shaded regions show 95% credible bands. The CAVI band (purple) is wider than the Gibbs band (pink), reflecting the different uncertainty propagation mechanisms: CAVI inflates the effective variance through the $\mathbb{E}_q[\beta^2]$ term in (20), which includes the variance of β , while the Gibbs band is computed conditionally on each posterior draw of β . The point estimates are virtually identical.

MIDAS Weight Profiles ($J=1$, Full Sample)

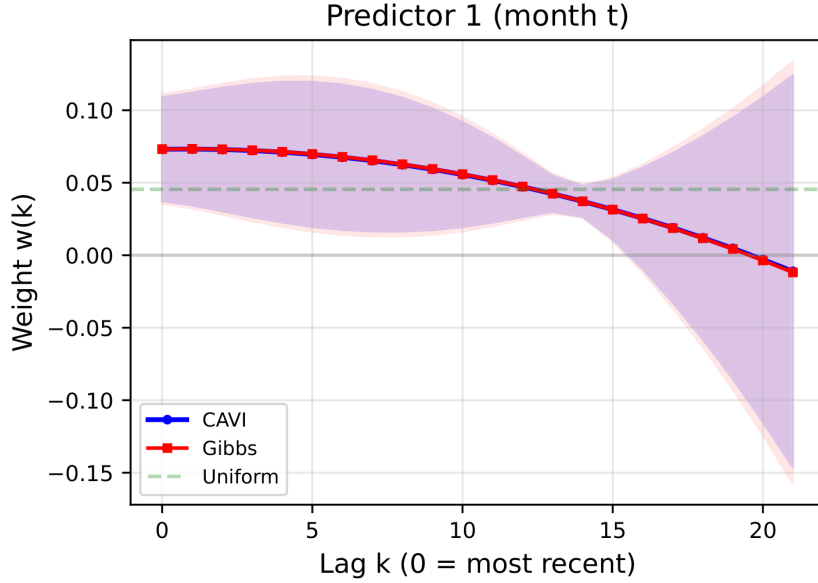


Figure 7: Estimated MIDAS weight profiles ($J = 1$, full sample). Blue: CAVI posterior mean. Red: Gibbs posterior mean. Shaded regions: 95% credible bands. Dashed green: uniform weights. Point estimates are virtually identical. The monotonically decreasing profile assigns greater weight to recent daily returns, consistent with the intuition that recent squared returns are more informative about current-month volatility.

The $J = 3$ specification tells a complementary story (Figure 9 in the Appendix): Predictor 1 (current month) retains the same decreasing profile, while Predictors 2 and 3 (months $t-1$ and $t-2$) have weights concentrated near zero with wide credible bands, indicating negligible marginal contribution—consistent with the modest forecasting gain of $J = 3$ over $J = 1$ (Table 4).

6 Conclusion

This paper develops the first variational inference algorithm for Bayesian MIDAS regression. The CAVI algorithm exploits conditional conjugacy of the linearly parameterized model to produce closed-form updates for all parameter blocks, propagating uncertainty across blocks through second moments and including a covariance correction specific to the MIDAS bilinear setting.

A Monte Carlo study across 21 configurations demonstrates that CAVI posterior means are essentially identical to those from a block Gibbs sampler—now confirmed through $J = 25$ —while achieving speedups of $107\times$ to $1,772\times$ (Table 9). Generic ADVI, by contrast, produces bias 7–14 times larger while being orders of magnitude slower, confirming that model-specific derivations are essential for this model class. Weight parameters are well-calibrated (coverage above 92%). Impact coefficient credible intervals exhibit mean-field

underdispersion, with coverage declining from 89% to 55% as predictor dimension grows—an honestly documented trade-off.

Three directions for future work follow naturally. First, extension to time-varying parameter MIDAS requires structured variational approximations (Loaiza-Maya et al., 2022) that capture temporal dependence—for example, targeting GDP nowcasting applications where parameter drift is economically motivated. Second, global-local shrinkage priors (Bayesian Lasso, horseshoe, Dirichlet-Laplace) can be incorporated with minimal additional derivation, enabling principled variable selection in large MIDAS panels. Third, stochastic volatility can be accommodated through the Gaussian approximation methods of Chan and Yu (2022).

References

- Blei, D.M., Kucukelbir, A. and McAuliffe, J.D. (2017). Variational inference: a review for statisticians. *Journal of the American Statistical Association*, 112(518), 859–877.
- Chan, J.C.C. and Jeliazkov, I. (2009). Efficient simulation and integrated likelihood estimation in state space models. *International Journal of Mathematical Modelling and Numerical Optimisation*, 1(1/2), 101–120.
- Chan, J.C.C. and Yu, X. (2022). Fast and accurate variational inference for large Bayesian VARs with stochastic volatility. *Journal of Economic Dynamics and Control*, 143, 104505.
- Chan, J.C.C., Poon, A. and Zhu, D. (2025). Time-varying parameter MIDAS models. *Journal of Econometrics*.
- Corsi, F. (2009). A simple approximate long-memory model of realized volatility. *Journal of Financial Econometrics*, 7(2), 174–196.
- Diebold, F.X. and Mariano, R.S. (1995). Comparing predictive accuracy. *Journal of Business & Economic Statistics*, 13(3), 253–263.
- Foroni, C., Marcellino, M. and Schumacher, C. (2015). Unrestricted mixed data sampling (MIDAS): MIDAS regressions with unrestricted lag polynomials. *Journal of the Royal Statistical Society: Series A*, 178(1), 57–82.
- Gefang, D., Koop, G. and Poon, A. (2020). Computationally efficient inference in large Bayesian mixed frequency VARs. *Economics Letters*, 191, 109120.
- Gefang, D., Koop, G. and Poon, A. (2023). Forecasting using variational Bayesian inference in large vector autoregressions with hierarchical shrinkage. *International Journal of Forecasting*, 39(1), 346–363.

- Giordano, R., Broderick, T. and Jordan, M.I. (2018). Covariances, robustness, and variational Bayes. *Journal of Machine Learning Research*, 19(51), 1–49.
- Ghysels, E., Santa-Clara, P. and Valkanov, R. (2006). Predicting volatility: getting the most out of return data sampled at different frequencies. *Journal of Econometrics*, 131(1-2), 59–95.
- Hoffman, M.D. and Gelman, A. (2014). The No-U-Turn Sampler: adaptively setting path lengths in Hamiltonian Monte Carlo. *Journal of Machine Learning Research*, 15, 1593–1623.
- Kohns, D. and Potjagailo, G. (2025). Flexible Bayesian MIDAS: time variation, group shrinkage and sparsity. *Journal of Business & Economic Statistics*, 43(4), 1034–1050.
- Kucukelbir, A., Tran, D., Ranganath, R., Gelman, A. and Blei, D.M. (2017). Automatic differentiation variational inference. *Journal of Machine Learning Research*, 18, 1–45.
- Loaiza-Maya, R., Smith, M.S., Nott, D.J. and Danaher, P.J. (2022). Fast and accurate variational inference for models with many latent variables. *Journal of Econometrics*, 230(2), 339–362.
- Mogliani, M. and Simoni, A. (2021). Bayesian MIDAS penalized regressions: estimation, selection, and prediction. *Journal of Econometrics*, 222(1), 833–860.
- Neal, R.M. (2003). Slice sampling. *Annals of Statistics*, 31(3), 705–767.
- Pettenuzzo, D., Timmermann, A. and Valkanov, R. (2016). A MIDAS approach to modeling first and second moment dynamics. *Journal of Econometrics*, 193(2), 315–334.
- Schumacher, C. (2014). MIDAS and bridge equations. *Discussion Paper No. 26/2014*, Deutsche Bundesbank.

Online Appendix

A.1 Proof of Proposition 2

Starting from the CAVI rule (15), the log-optimal density for $\boldsymbol{\eta}_j$ involves isolating terms dependent on $\boldsymbol{\eta}_j$ from the expected log-joint. Writing $e_t = e_t^{(-j)} - \beta_j \mathbf{r}_t^{(j)\top} \boldsymbol{\eta}_j$ and expanding:

The quadratic term in $\boldsymbol{\eta}_j$ gives

$$-\frac{1}{2} \mathbb{E}_q[\sigma^{-2}] \mathbb{E}_q[\beta_j^2] \sum_t \boldsymbol{\eta}_j^\top \mathbf{r}_t^{(j)} \mathbf{r}_t^{(j)\top} \boldsymbol{\eta}_j - \frac{1}{2} \sigma_\eta^{-2} \boldsymbol{\eta}_j^\top \boldsymbol{\eta}_j,$$

yielding the precision matrix (20).

For the linear term, the key calculation is $\mathbb{E}_q[\beta_j \cdot e_t^{(-j)}]$. Since $\beta_j = \mathbf{e}_{j+1}^\top \boldsymbol{\xi}$:

$$\begin{aligned} \mathbb{E}_q[\beta_j (y_t - \mathbf{g}_t^\top \boldsymbol{\xi})] &= \mu_{\beta_j} y_t - \mathbf{g}_t^\top \mathbb{E}_q[\boldsymbol{\xi} \boldsymbol{\xi}^\top] \mathbf{e}_{j+1} \\ &= \mu_{\beta_j} y_t - \mathbf{g}_t^\top (\boldsymbol{\mu}_\xi \boldsymbol{\mu}_\xi^\top + \boldsymbol{\Sigma}_\xi) \mathbf{e}_{j+1} \\ &= \mu_{\beta_j} \bar{e}_t^{(-j)} - \mathbf{g}_t^\top \boldsymbol{\Sigma}_\xi \mathbf{e}_{j+1}, \end{aligned}$$

where the last term is the covariance correction. Collecting and applying $\boldsymbol{\mu}_{\eta_j} = \boldsymbol{\Sigma}_{\eta_j} \times$ (linear coefficient) yields (21). \square

A.2 ELBO computation

The ELBO decomposes as:

Expected log-likelihood:

$$\mathbb{E}_q[\log p(\mathbf{y} \mid \boldsymbol{\xi}, \boldsymbol{\eta}, \sigma^2)] = -\frac{T}{2} \log(2\pi) - \frac{T}{2} (\log \tilde{b} - \psi(\tilde{a})) - \frac{\tilde{a}}{2\tilde{b}} \sum_t \mathbb{E}_q[e_t^2].$$

Expected log-priors:

$$\begin{aligned} \mathbb{E}_q[\log p(\boldsymbol{\xi})] &= -\frac{J+1}{2} \log(2\pi) - \frac{1}{2} \log |\boldsymbol{\Lambda}_\xi^{-1}| - \frac{1}{2} \text{tr}(\boldsymbol{\Lambda}_\xi (\boldsymbol{\mu}_\xi \boldsymbol{\mu}_\xi^\top + \boldsymbol{\Sigma}_\xi)), \\ \mathbb{E}_q[\log p(\boldsymbol{\eta}_j)] &= -\frac{P_j-1}{2} \log(2\pi \sigma_\eta^2) - \frac{1}{2\sigma_\eta^2} (\|\boldsymbol{\mu}_{\eta_j}\|^2 + \text{tr}(\boldsymbol{\Sigma}_{\eta_j})), \\ \mathbb{E}_q[\log p(\sigma^2)] &= a_0 \log b_0 - \log \Gamma(a_0) - (a_0 + 1) (\log \tilde{b} - \psi(\tilde{a})) - b_0 \tilde{a} / \tilde{b}. \end{aligned}$$

Entropies:

$$\begin{aligned} H[q(\boldsymbol{\xi})] &= \frac{J+1}{2} (1 + \log(2\pi)) + \frac{1}{2} \log |\boldsymbol{\Sigma}_\xi|, \\ H[q(\boldsymbol{\eta}_j)] &= \frac{P_j-1}{2} (1 + \log(2\pi)) + \frac{1}{2} \log |\boldsymbol{\Sigma}_{\eta_j}|, \\ H[q(\sigma^2)] &= \tilde{a} + \log(\tilde{b} \Gamma(\tilde{a})) - (1 + \tilde{a}) \psi(\tilde{a}). \end{aligned}$$

A.3 Additional Monte Carlo results

Table 5: Robustness results (Tier 2, Panel A): Weight profile shapes. $T = 200$, $J = 3$, $P = 3$.

Profile	Method	Bias(β)	Cov95(β)	Bias(η)	Cov95(η)	ESS
Decreasing	CAVI	0.051	0.749	0.012	0.921	—
Decreasing	Gibbs	0.077	0.900	0.023	0.946	643
Hump-shaped	CAVI	0.057	0.819	0.010	0.942	—
Hump-shaped	Gibbs	0.079	0.899	0.019	0.961	1,034
U-shaped	CAVI	0.064	0.827	0.006	0.962	—
U-shaped	Gibbs	0.086	0.891	0.009	0.970	1,108

Table 6: Robustness (Panel B): Signal-to-noise ratio and frequency ratio.

Variation	Method	Bias(β)	Cov95(β)	Bias(η)	Cov95(η)	ESS
$\sigma_0^2 = 0.25$ (high SNR)	CAVI	0.010	0.899	0.001	0.948	—
	Gibbs	0.012	0.953	0.002	0.959	3,280
$\sigma_0^2 = 4$ (low SNR)	CAVI	0.112	0.747	0.011	0.943	—
	Gibbs	0.148	0.861	0.011	0.966	883
$K = 5$ (quarterly)	CAVI	0.079	0.793	0.010	0.936	—
	Gibbs	0.112	0.867	0.009	0.957	696
$K = 65$ (daily)	CAVI	0.332	0.483	0.012	0.952	—
	Gibbs	0.523	0.497	0.008	0.981	270

Table 7: Stress test results (Tier 3).

T	J	Method	Bias(β)	RMSE(β)	Cov95(β)	Bias(η)	Cov95(η)	ESS
50	10	CAVI	0.240	0.383	0.374	0.068	0.957	—
50	10	Gibbs	0.266	0.382	0.842	0.059	0.993	366
200	10	CAVI	0.156	0.273	0.441	0.026	0.955	—
200	10	Gibbs	0.203	0.293	0.708	0.016	0.981	339
50	3	CAVI	0.350	0.573	0.455	0.038	0.933	—
50	3	Gibbs	0.433	0.599	0.783	0.048	0.980	646

A.4 Prior and initialization sensitivity

Prior sensitivity. Table 8 reports CAVI performance under three settings of the prior variance $\sigma_\beta^2 \in \{5, 10, 20\}$ for the impact coefficients, with $J = 3$, $T = 200$, 100 replications. Results are virtually identical across specifications, confirming robustness to the choice of prior variance over a fourfold range.

Table 8: Prior sensitivity: CAVI performance under different σ_β^2 . $J = 3$, $T = 200$, 100 replications.

σ_β^2	Bias(β)	RMSE(β)	Cov95(β)	Bias(η)	Cov95(η)
5	0.128 (.007)	0.140 (.008)	0.875 (.033)	0.021	0.932
10	0.128 (.007)	0.140 (.008)	0.880 (.032)	0.021	0.932
20	0.127 (.007)	0.140 (.008)	0.880 (.032)	0.021	0.932

Initialization sensitivity. We compare the default OLS warm-start initialization against random initialization ($\mu_\xi \sim \mathcal{N}(\mathbf{0}, 0.01\mathbf{I})$, $\mu_{\eta_j} \sim \mathcal{N}(\mathbf{0}, 0.01\mathbf{I})$) over 50 replications with $J = 3$, $T = 200$. OLS initialization yields substantially better results: mean absolute bias of 0.121 (SE 0.011) versus 0.634 (SE 0.071) for random initialization, with the maximum ELBO difference across replications reaching 76.3. This sensitivity arises because the ELBO landscape of the bilinear model has multiple local optima; the OLS warm-start directs the algorithm toward the basin containing the global optimum. We recommend OLS initialization as the default for all applications.

A.5 Computational timing

Table 9 reports the mean CAVI and Gibbs estimation times across all Monte Carlo configurations, together with speedup factors and the minimum effective sample size (ESS) of the Gibbs chain. The speedup ranges from $107\times$ ($J = 25$, 50 replications) to $1,772\times$ ($J = 1$). For $J = 50$, Gibbs timing is not reported as the computational cost was prohibitive.

Table 9: Computational timing across Monte Carlo configurations. CAVI and Gibbs times are per-fit averages (500 replications except $J = 25$ Gibbs: 50 replications).

Config	CAVI (s)	Iters	Gibbs (s)	Speedup	Min ESS
1A-1 ($J=1$)	0.001	3	1.82	$1,772\times$	4,103
1A-2 ($J=3$)	0.006	10	3.59	$645\times$	1,066
1A-3 ($J=5$)	0.023	29	6.54	$283\times$	701
1A-4 ($J=10$)	0.066	37	15.56	$238\times$	539
1A-5 ($J=25$)	0.322	49	34.44	$107\times$	134
1A-6 ($J=50$)	1.383	67	—	—	—
2D-3 ($K=65$)	0.030	59	4.06	$136\times$	270

A.6 ELBO values

Table 10 reports the final ELBO values across all Monte Carlo configurations. The ELBO increases (becomes less negative) with higher SNR and decreases with more predictors, as expected from the additional model complexity.

Table 10: Final ELBO values across Monte Carlo configurations (500 replications).

Config	Mean	Std	Min	Max
1A-1 ($J=1$)	-235.0	10.1	-264.9	-210.6
1A-2 ($J=3$)	-253.5	9.5	-285.0	-220.1
1A-3 ($J=5$)	-263.7	9.5	-290.0	-228.5
1A-4 ($J=10$)	-291.3	9.8	-318.3	-263.9
1A-5 ($J=25$)	-370.9	8.2	-390.8	-338.2
1A-6 ($J=50$)	-503.5	7.7	-527.3	-480.0
2B-1 (high SNR)	-100.6	9.8	-130.4	-70.1
2B-2 (low SNR)	-318.2	9.6	-345.4	-286.8

A.7 Additional figures

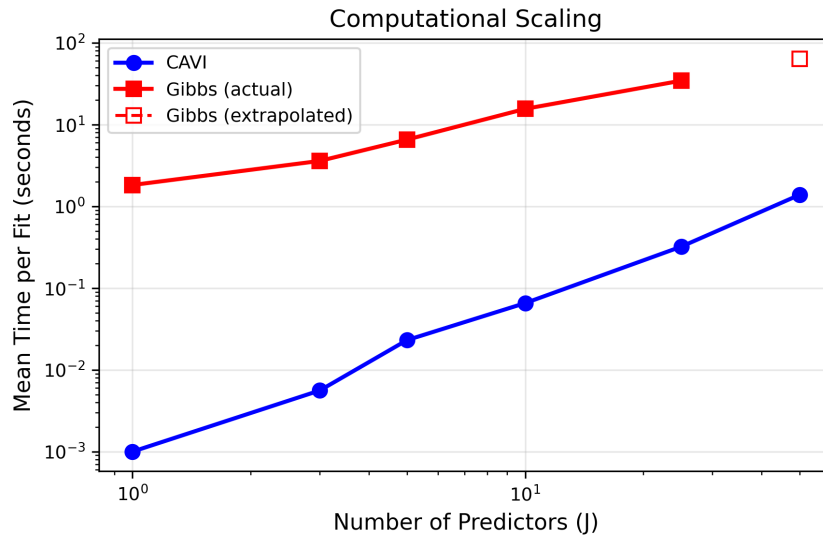


Figure 8: Computational scaling: mean estimation time per fit as a function of J (log-log scale). Blue: CAVI. Red: Gibbs (solid: measured; open: extrapolated). The gap widens with J due to Gibbs mixing degradation.

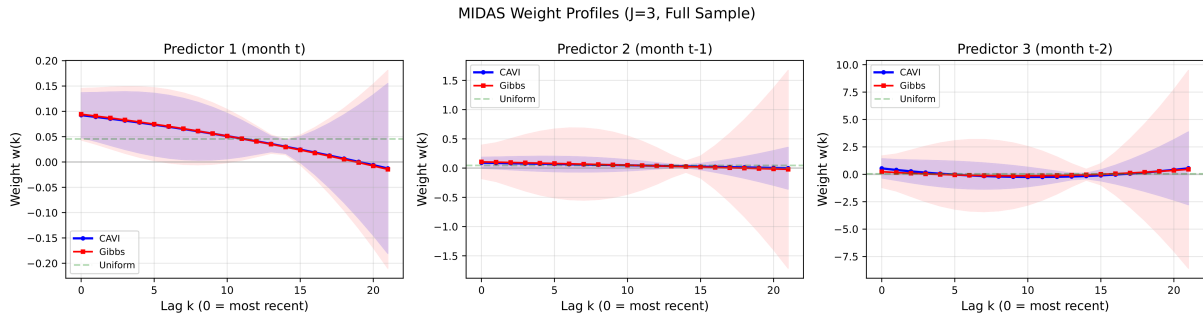


Figure 9: Estimated MIDAS weight profiles ($J = 3$, full sample). Left: Predictor 1 (month t) shows a monotonically decreasing profile with tight credible bands, consistent with the $J = 1$ result (Figure 7). Center and Right: Predictors 2 and 3 (months $t-1$ and $t-2$) have weights concentrated near zero with wide credible bands, indicating negligible marginal contribution beyond the current month’s squared returns. CAVI (blue) and Gibbs (red) point estimates are virtually identical across all three predictors.

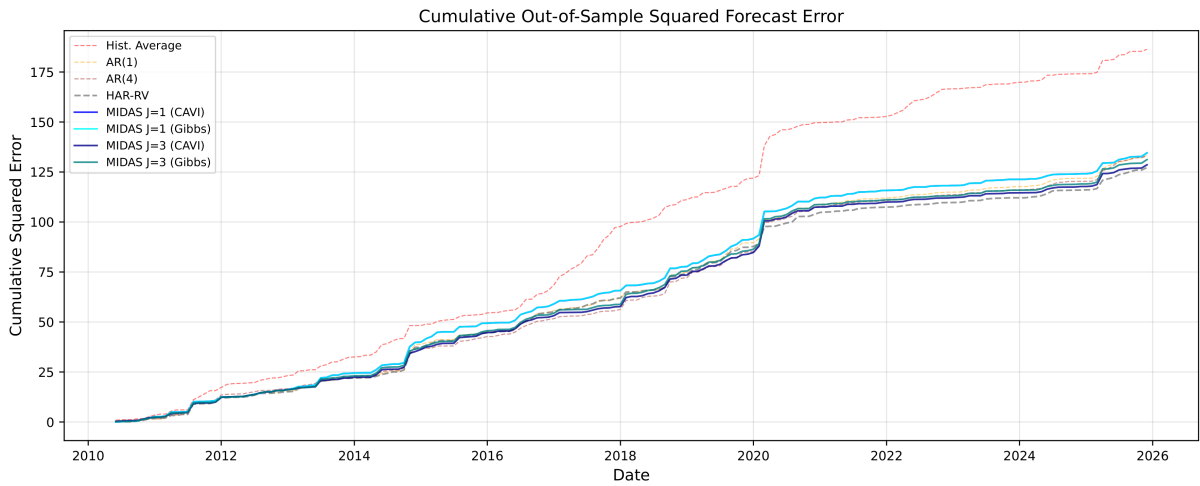


Figure 10: Cumulative out-of-sample squared forecast error (2010–2025). The historical average (pink) is clearly dominated. All other models cluster closely, with a sharp increase around March 2020 (COVID-19). MIDAS $J = 3$ (CAVI) tracks HAR-RV most closely.

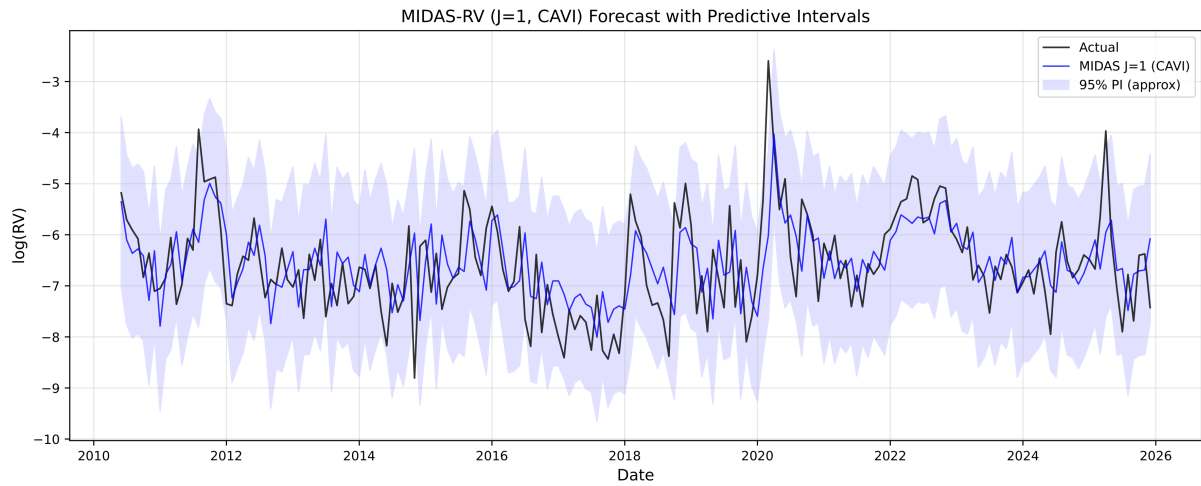


Figure 11: MIDAS-RV ($J = 1$, CAVI) out-of-sample forecasts with approximate 95% predictive intervals. The March 2020 COVID-19 spike falls outside the interval, as expected for an extreme tail event.